Enhanced ENSO-Unrelated Summer Variability in the Indo–Western Pacific under Global Warming

CHUAN-YANG WANG,[a,b] XIAO-TONG ZHENG,[a,b] AND SHANG-PING XIE[c]

[a] *Frontier Science Center for Deep Ocean Multispheres and Earth System and Key Laboratory of Physical Oceanography, Ocean University of China, Qingdao, China*
[b] *Laoshan Laboratory, Qingdao, China*
[c] *Scripps Institution of Oceanography, University of California San Diego, La Jolla, California*

(Manuscript received 21 June 2022, in final form 12 October 2022)

ABSTRACT: El Niño–Southern Oscillation (ENSO) is an important but not the only source of interannual variability over the Indo–western Pacific. Non-ENSO forced variability in the region has received recent attention because of the implications for rainy-season prediction. Using a 35-member CESM1 Large Ensemble (CESM-LE) and 30 CMIP6 models, this study shows that the ensemble means project intensified interannual variability for precipitation, low-level winds, and sea level pressure under global warming, associated with the enhanced large-scale anomalous anticyclone (AAC) over the tropical northwestern (NW) Pacific after the ENSO signal is removed. A decomposition based on the column water vapor budget reveals that enhanced precipitation variability is due to the increased background specific humidity. The resultant anomalous diabatic heating intensifies the AAC, which further strengthens the precipitation anomalies. Over the tropical NW Pacific, the wind-induced evaporative cooling on the southeastern flank of the AAC is countered by the increased shortwave radiation due to the strengthened precipitation reduction. Tropospheric temperature anomalies in the ensemble means show no significant change, suggesting no apparent change of the interbasin positive feedback between the AAC and northern Indian Ocean SST. Intermodel analysis based on CMIP6 reveals that models with a larger increase in ENSO-unrelated precipitation variability over the NW Pacific are associated with stronger background warming in the eastern equatorial Pacific, due to the modulated Walker and Hadley circulations.

KEYWORDS: Atmosphere-ocean interaction; Climate change; Climate variability; Interannual variability

1. Introduction

Summer is the major rainy season in South and East Asia, home to some 3 billion people. Often excited by El Niño, a low-level anomalous anticyclone (AAC) forms in the boreal winter and persists into the following summer (e.g., Zhang et al. 1996; Wang et al. 2003; Xie et al. 2009), accompanied by anomalous sea surface temperature (SST) in the tropical Indian Ocean (IO) and northwestern (NW) Pacific. The AAC has a great impact on the interannual variability of the Indo–western Pacific summer climate by modulating atmospheric circulation and moisture transport (e.g., Du et al. 2011; Xie et al. 2016; Hu et al. 2017).

The relationship between El Niño–Southern Oscillation (ENSO) and the AAC has been extensively studied. It is commonly agreed that the AAC is excited by ENSO and maintained by ocean–atmosphere interactions. Early studies suggest that wind–evaporation–SST (WES) feedback over the tropical NW Pacific is important for the formation of the AAC during the El Niño mature winter and helps it persist into the following summer (Wang et al. 2000). The anomalous easterlies associated with the AAC strengthen the background trades over the tropical NW Pacific, increasing evaporation and cooling the ocean. The negative SST anomalies then suppress local convection and enhance the AAC via atmospheric Rossby wave response. An alternative theory emphasizes the role of the IO SST anomalies in the summer, called the IO capacitor effect (Yang et al. 2007). El Niño first warms the IO via a series of teleconnection processes (Klein et al. 1999; Alexander et al. 2002; Xie et al. 2002; Wu et al. 2008; Du et al. 2009) and the warm SST forces an eastward propagating Kelvin wave (Matsuno 1966; Gill 1980), suppressing convection and strengthening the AAC over the tropical NW Pacific by inducing Ekman divergence in the lower troposphere (Xie et al. 2009). Further studies show that the low-level easterly anomalies extend over the north Indian Ocean, weakening the background southwesterly monsoon, and warming the upper ocean (Du et al. 2009). The warm SST in the tropical IO and the AAC then form an interbasin positive feedback (Kosaka et al. 2013; Wang et al. 2013). The coherent spatial pattern of oceanic and atmospheric anomalies in the ENSO decay summer has thus been named the Indo–western Pacific Ocean Capacitor (IPOC; Xie et al. 2016).

The response of the IPOC to global warming has received much recent attention. The change in the ENSO-induced IPOC is determined by both the changes in ENSO amplitude and the IPOC–ENSO relationship. The ENSO amplitude effect is straightforward as a stronger El Niño event tends to

Denotes content that is immediately available upon publication as open access.

Supplemental information related to this paper is available at the Journals Online website: https://doi.org/10.1175/JCLI-D-22-0450.s1.

Corresponding author: Xiao-Tong Zheng, zhengxt@ouc.edu.cn

DOI: 10.1175/JCLI-D-22-0450.1

excite stronger anomalies of SST, precipitation, and circulation over the Indo–western Pacific region. The change in the IPOC–ENSO relationship, on the other hand, is more complicated and hence becomes the focus of many recent studies. Some argue that the El Niño–induced tropical IO warming is enhanced under global warming, which leads to an enhanced IO capacitor effect and strengthened AAC (Zheng et al. 2011; Hu et al. 2014). Other studies suggest that the summer AAC is likely to weaken under anthropogenic forcing due to the decreased SST gradient between the NW Pacific and tropical IO (Jiang et al. 2018) or to the increased atmospheric boundary layer static stability over the tropical IO (He et al. 2019). The change of the summer AAC can be further complicated by the decay rate of the projected ENSOs (Jiang et al. 2019; Wu et al. 2020, 2021). A fast decaying El Niño event is often followed by negative SST anomalies in the tropical central Pacific in summer, reinforcing the AAC via Rossby wave response (Fan et al. 2013; Chen et al. 2016). Those changes in the IPOC–ENSO relationship are often associated with changes in ENSO properties, such as the magnitude, frequency, spatial distribution, and seasonality, all have been shown to have large uncertainties in future projections (e.g., Yeh et al. 2009; Collins et al. 2010; Kim and Jin 2011; Kim et al. 2014; Zheng et al. 2018; Ying et al. 2019; Cai et al. 2021).

Recent studies reveal that the ocean–atmosphere interactions that sustain the IPOC can operate without direct ENSO forcing (Kosaka et al. 2013; Xie et al. 2016; Wang et al. 2020). In fact, the recurrent oceanic and atmospheric anomalies associated with the ENSO-unrelated IPOC have a large impact on the Indo–western Pacific climate on multiple time scales (Wang et al. 2018, 2021). In the summer of 2020, an IPOC event without El Niño forcing led to historic mei-yu–baiu rainfall and Yangtze flooding (Zhou et al. 2021; Lu and Takaya 2021). It is unclear if this kind of internal (ENSO-unrelated) IPOC will increase in the future, as its change under global warming remains largely unexplored.

This study aims to investigate the change in the ENSO-unrelated Indo–western Pacific summer variability, specifically the IPOC mode, under global warming. Using state-of-the-art coupled general circulation models (CGCMs), we focus on key oceanic and atmospheric processes that are important for the warming-induced change in IPOC variability. We show that in a warmer climate, the ENSO-unrelated summer AAC intensifies despite little change in the SST anomalies. The increased background water vapor intensifies the positive feedback between the AAC and precipitation anomalies.

The rest of the paper is organized as follows. Section 2 describes the data and methods used in this study. Section 3 shows how the ENSO-unrelated summer interannual variability over the Indo–western Pacific region changes under global warming, with a focus on the ENSO-unrelated IPOC. Section 4 investigates the change of the specific oceanic and atmospheric processes associated with the change of the ENSO-unrelated IPOC in the ensemble mean of a set of large ensemble simulations. Section 5 explores the intermodel variability of the internal IPOC and the associated SST warming pattern. Section 6 discusses the potential climate impact of the ENSO-unrelated IPOC under global warming. Section 7 is the summary.

2. Data and methods

a. Datasets

We analyze the outputs of the Community Earth System Model Large Ensemble (CESM-LE; Kay et al. 2015) and 30 phase 6 of the Coupled Model Intercomparison Project (CMIP6; Eyring et al. 2016) models. In CESM-LE, the first 35 members are used while one realization (usually r1i1p1f1) of each CMIP6 model is used to compose an ensemble of 30 members (models used are shown in Table 1). Historical simulations for 1950–99 are adopted as the baseline for current climate, and the 50-yr period of 2045–94 from the Representative Concentration Pathway 8.5 (RCP85) simulations for the CESM-LE and Shared Socioeconomic Pathway 5 (SSP5–85) simulations for the CMIP6 models are used as the projected future scenarios. All datasets are first interpolated onto a common 2.5° × 2.5° grid for intermodel comparison. A nine-point Lanczos high-pass filter with half-power at 9 years is applied onto all variables at each grid point to remove decadal variability and long-term trends during both historical and future simulations. The appendix briefly discusses the model performance in simulating the ENSO-forced and ENSO-unrelated IPOC.

b. Extraction of the ENSO-unrelated variability

This study focuses on the seasonally averaged interannual variability of Indo–western Pacific climate in boreal summer [June–August (JJA)]. We employ a multilinear regression method to remove the ENSO signal from the CESM-LE and CMIP6 simulations. The anomaly y satisfies $y(t) = aP_{\mathrm{DJF}}(t) + bP_{\mathrm{JJA}}(t) + c(t)$, where P_{DJF} and P_{JJA} denote the Niño-3.4 index for the preceding winter [December–February (DJF)] and concurrent summer (JJA), respectively, with a and b being their respective regression coefficients. The first two terms on the right-hand side represent the ENSO-forced variability and the third term $c(t)$ denotes the ENSO-unrelated variability. The relationship between the winter Niño-3.4 and the Indo–western Pacific anomalies in the following summer has been well established (Xie et al. 2016; Zheng 2019), and we further include the concurrent summer Niño-3.4 index to account for the potential enhancement of the AAC associated with the fast-decaying ENSO events (Jiang et al. 2019; Wu et al. 2020; He et al. 2022). Both the ENSO-forced and ENSO-unrelated variability feature the anomalous anticyclone associated with suppressed precipitation over the NW Pacific (see appendix). A similar regression method has been used in our previous studies, showing that $c(t)$ can well capture the ENSO-unrelated interannual variability over the NW Pacific region (Wang et al. 2018). We refer to the ENSO-unrelated component $c(t)$ of the IPOC as the "internal IPOC" as it is mainly maintained by ocean–atmosphere interactions internal to the Indo–western Pacific region (Kosaka et al. 2013; Xie et al. 2016; Wang et al. 2020).

3. Increased interannual variability in the Indo–western Pacific

We first investigate the ENSO-unrelated component of the summer (JJA) interannual variability in the Indo–western

TABLE 1. CMIP6 models used in this study.

No.	Name	Institution	No.	Name	Institution
1	ACCESS-CM2	Commonwealth Scientific and Industrial Research Organisation	16	GFDL-ESM4	National Oceanic and Atmospheric Administration, Geophysical Fluid Dynamics Laboratory
2	ACCESS-ESM1-5	Commonwealth Scientific and Industrial Research Organisation and Australian Research Council Centre of Excellence for Climate System Science	17	GISS-E2-1-G	Goddard Institute for Space Studies
3	BCC-CSM2-MR	Beijing Climate Center	18	INM-CM4-8	Institute for Numerical Mathematics, Russian Academy of Science
4	CAMS-CSM1-0	Chinese Academy of Meteorological Sciences	19	INM-CM5-0	
5	CanESM5-CanOE	Canadian Centre for Climate Modelling and Analysis	20	IPSL-CM6A-LR	Institut Pierre Simon Laplace
6	CESM2	National Center for Atmospheric Research	21	KACE-1-0-G	National Institute of Meteorological Sciences/Korea Meteorological Administration, Climate Research Division
7	CESM2-WACCM		22	MIROC6	Japan Agency for Marine-Earth Science and Technology, Atmosphere and Ocean Research Institute, The University of Tokyo, National Institute for Environmental Studies and RIKEN Center for Computational Science
8	CNRM-CM6-1	Centre National de Recherches Meteorologiques and Centre Europeen de Recherche et de Formation Avancee en Calcul Scientifique	23	MIROC-ES2L	
9	CNRM-CM6-1-HR		24	MPI-ESM1-2-HR	Max Planck Institute for Meteorology
10	CNRM-ESM2-1		25	MPI-ESM1-2-LR	
11	EC-Earth3	EC-Earth-Consortium	26	MRI-ESM2-0	Meteorological Research Institute
12	EC-Earth3-Veg		27	NESM3	Nanjing University of Information and Technology
13	FGOALS-f3-L	Chinese Academy of Sciences	28	NorESM2-LM	Norwegian Climate Centre
14	FGOALS-g3		29	NorESM2-MM	
15	GFDL-CM4	National Oceanic and Atmospheric Administration, Geophysical Fluid Dynamics Laboratory	30	UKESM1-0-LL	Met Office Hadley Centre

Pacific region under global warming. Precipitation, sea level pressure (SLP), and 850-hPa zonal winds all show strong interannual variability over the tropical-to-subtropical Indo–western Pacific, in both historical (contours in Fig. 1) and future simulations (not shown). Specifically, all the variables show regional maxima over the subtropical NW Pacific, highlighting the role of the internal IPOC in modulating the summer climate variability in this region (Wang et al. 2018).

The change in the ENSO-unrelated interannual variability is also shown in Fig. 1, represented by the difference in the interannual standard deviation of the future relative to the historical simulations. In CESM-LE, the internal variability of the precipitation, SLP, and 850-hPa zonal winds all increase in the NW Pacific region under global warming. Specifically, the maximum change in SLP is centered over the subtropical NW Pacific, with increased zonal wind variability on both the poleward and equatorward flanks. This suggests that the internal IPOC may become more active and responsible for the increased interannual variability in the future. The change in precipitation interannual variability is collocated with the center of the circulation change over the NW Pacific, further indicating a strengthened internal IPOC mode. The SST variability, on the other hand, shows very small change in the NW Pacific (Figs. 1g,h). The mismatched changes in atmospheric and oceanic variability may suggest altered ocean–atmosphere interactions in a warmer climate as discussed in the next section.

Over the tropical IO, interannual variability of SLP shows no significant change while precipitation increases over the northern IO and South and Southeast Asia. The zonal winds, on the other hand, show weakened interannual variability over the Arabian Sea. Interestingly, the SST variability increases dramatically in the eastern equatorial IO, while the zonal wind variability decreases along the equator. This is possibly related to the change of the Indian Ocean Dipole mode, due to shallowed background thermocline and

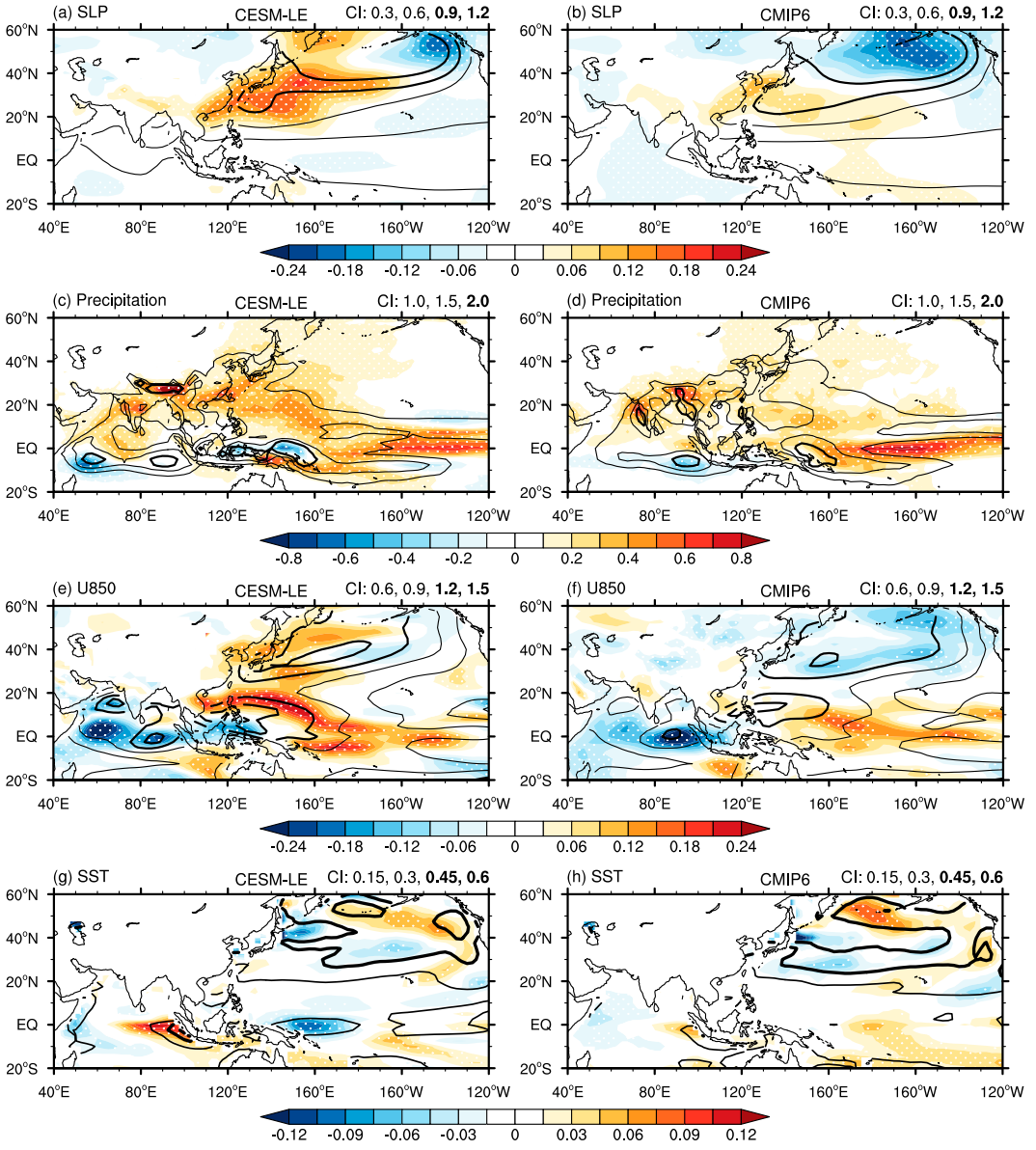

FIG. 1. Changes in ENSO-unrelated interannual standard deviation (color shading) in future projection (2046–95) relative to historical simulations (1950–99) in (a),(b) SLP (unit: hPa), (c),(d) precipitation (unit: mm day^{-1}), (e),(f) 850-hPa zonal winds (unit: m s^{-1}), and (g),(h) SST (unit: K) in (left) CESM-LE and (right) CMIP6 in JJA. Black contours show the standard deviation in the historical simulations, with the contour levels labeled at the top right of each panel. Boldface text corresponds to the thickened contours. Stippling indicates 70% of the members in each ensemble agree on the signs of the changes.

intensified atmospheric static stability (e.g., Zheng et al. 2010, 2021). The change simulated by CMIP6 broadly agrees with CESM-LE in the Indo–western Pacific region but with smaller magnitude.

SLP, precipitation, and wind variability all increase under global warming, but with different magnitudes relative to their respective historical levels. We have computed the regionally averaged SLP (10°–35°N, 120°–160°E), precipitation (10°–25°N, 140°–170°E), and relative vorticity (10°–35°N, 120°–160°E) indices over the NW Pacific region. The interannual standard deviation increases by 18% (10%), 11% (1.2%), and 39% (21%) for NW Pacific SLP, relative vorticity, and precipitation, respectively, in CESM-LE (CMIP6). The change in precipitation variability is much larger than those in SLP and relative vorticity (Fig. 2). By contrast, the SST in both the northern IO and NW Pacific shows no apparent change.

The CMIP6 ensemble mean agrees with the results of the CESM-LE but with a smaller magnitude. It is also worth mentioning that the intermember spread (measured by

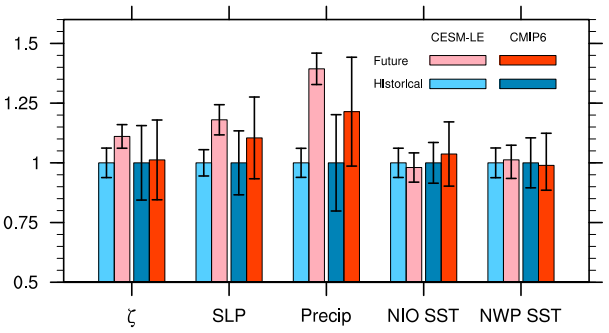

FIG. 2. Regionally averaged ENSO-unrelated interannual variability of NW Pacific relative vorticity (ζ; averaged over 10°–35°N, 120°–160°E), SLP (averaged over 10°–35°N, 120°–160°E), precipitation (averaged over 10°–25°N, 140°–170°E), tropical northern IO SST (averaged over 5°–20°N, 50°–120°E), and tropical NW Pacific SST (averaged over 5°–20°N, 140°–170°E) for both historical and future experiments. All indices are first normalized by their respective ensemble-mean value of the historical simulations, and the error bars indicates the intermember standard deviation.

intermember standard deviation; Fig. 2) of the CMIP6 ensemble is much larger than that of the CESM-LE, implying that the intermodel uncertainty has large contribution to the uncertainty in the future projection of the ENSO-unrelated variability. The intermodel uncertainty may be associated with the uncertainty of the changes in the climatological SST, winds, precipitation, and water vapor, etc., under global warming across the CMIP6 ensemble. In the next two sections, we will focus on the ensemble-mean results projected by the CESM-LE and the intermodel spread of the CMIP6.

4. Change of the internal IPOC in CESM-LE

a. *Strengthened anomalies associated with the internal IPOC*

To illustrate the change of the internal IPOC and the ocean–atmosphere interactions involved, we compute the regression coefficients of the SST, winds, precipitation, and SLP anomalies against the normalized NW Pacific SLP index over the Indo–western Pacific region (Wang et al. 2018, 2020). The SLP index tracks the AAC, which is an intrinsic atmospheric mode that grows on the confluence of the monsoon westerly and easterly trade winds (Hu et al. 2019; Wang et al. 2021; Xie 2023). Here we use a normalized SLP index so both the change in magnitude and spatial distribution of the anomalies can be captured by the regression coefficients, as the interannual variability of the NW Pacific SLP increases in the CESM-LE future projections (Figs. 1 and 2). In CESM-LE, the ensemble means in historical and future experiments show clear IPOC-like distributions (Fig. 3). The anomalous anticyclone accompanied by suppressed convection is located in the NW Pacific, with positive (negative) SST anomalies in the northern IO (NW Pacific), consistent with previous studies (Kosaka et al. 2013; Xie et al. 2016).

To demonstrate the change of the internal IPOC variability in a warmer climate, we subtract the regression coefficients of the historical simulations from the future projections (Figs. 3e,f). The SLP anomalies over the NW Pacific increase in a warmer climate as suggested by the increased interannual variability (Figs. 1 and 2). The accompanied easterly anomalies strengthen on the southern flank of the AAC while weaken over the Arabian Sea (Fig. 3e), also consistent with the change of the zonal wind variabilities (Fig. 1e). The negative precipitation anomalies over the NW Pacific strengthen in the future projections (Fig. 3f), suggesting enhanced precipitation variability over this region. Overall, the spatial distribution of the internal-IPOC-induced changes in SLP, low-level winds and precipitation largely resemble the corresponding changes in their interannual variability, highlighting the importance of the internal IPOC in the Indo–western Pacific summer climate variability.

The SST anomalies associated with the internal IPOC, on the other hand, increase in the Bay of Bengal and South China Sea, but weaken east of the Philippine and in the Kuroshio Extension region (Fig. 3e). The strengthened SST anomalies in the tropical northern IO are associated with enhanced easterlies (Fig. 4) induced by the strengthened internal IPOC, as the anomalous easterlies weaken the background monsoonal southwesterlies (Kosaka et al. 2013; Wang et al. 2020). An intermember (intermodel) analysis indeed finds that the changes in northern IO SST are highly correlated with the changes in the anomalous easterlies (Fig. S1 in the online supplemental material). Interestingly, over the tropical NW Pacific, the weakened negative SST anomalies are accompanied by enhanced negative precipitation and easterly wind anomalies. Such changes in winds and precipitation against the SST contradict the WES feedback, seemingly indicating a weakened ocean–atmosphere coupling, as will be discussed in section 4c.

The regionally averaged regression coefficients are shown in Fig. 4. As discussed above, the regression coefficients of NW Pacific zonal winds and precipitation both increase in the future experiments, but with different magnitudes. The anomalous 850-hPa zonal winds over the NW Pacific associated with the internal IPOC increase by ~21% while the precipitation anomalies over the NW Pacific increase by ~52% in the ensemble mean of the CESM-LE. The regression coefficient of the NW Pacific SST, on the other hand, decreases by ~6%. The tropospheric temperature (TT) anomalies over the tropical IO are small in both historical and future experiments and show no significant change. While Wang et al. (2018) reported that the TT anomalies associated with the internal IPOC are weaker than the ENSO-forced one in observations, the diminishingly small regression coefficients of TT in CESM-LE are probably due to model bias (see appendix).

The comparison between the change in the NW Pacific SST, precipitation, wind anomalies, and the change in the tropical IO TT anomalies suggests that the intensified AAC over the NW Pacific is mainly contributed by local feedbacks. Namely, the enhanced precipitation deficit intensifies the diabatic cooling effect on the atmosphere, strengthening the AAC. On the other hand, increased static stability in a warmer climate (Knutson and Manabe 1995; Held and Soden 2006; Ma et al. 2012; P. Huang et al. 2017) weakens the

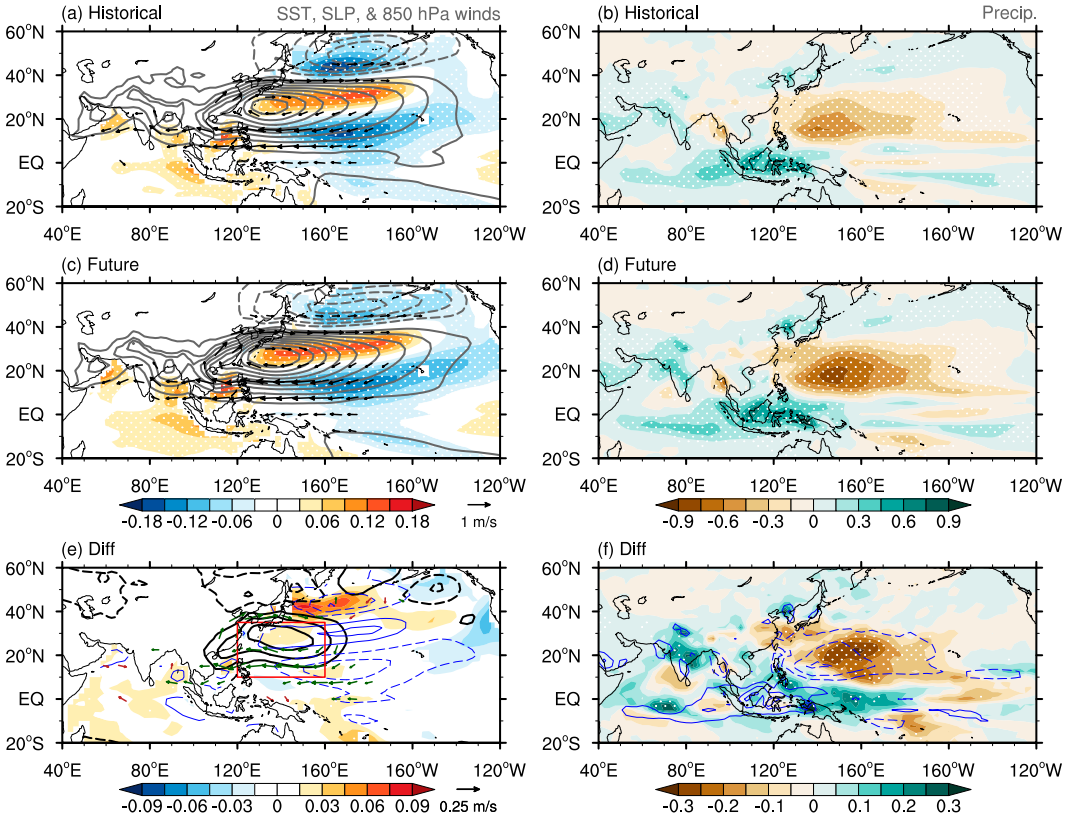

FIG. 3. CESM-LE ensemble mean of the JJA anomalies of (a),(c) SST (color shading; K), SLP (black contours; every 0.1 hPa, with zero line omitted), 850-hPa wind velocity (arrows), and (b),(d) precipitation (unit: mm day^{-1}) associated with internal IPOC, represented by the regression coefficients against normalized NW Pacific SLP index (averaged over 10°–35°N, 120°–160°E) in (a),(b) historical and (c),(d) future experiments. (e),(f) The changes in the anomalies superimposed on SST and precipitation of the historical simulations (blue contours, at ±0.06, ±0.12, … K for SST and ±0.3, ±0.6, … mm day^{-1} for precipitation). Green and brown arrows indicate increased and reduced zonal wind anomalies in the future projections, respectively, and stippling indicates 70% of the members agree on the sign of the shaded anomalies.

circulation response to the anomalous heating, causing disproportionate changes in the precipitation and circulation anomalies.

b. *Diagnostics of the changes in precipitation variability*

To examine the changes in precipitation anomalies associated with internal IPOC, we adopt the methods of Huang and Xie (2015) to decompose the change in precipitation anomalies ($\Delta P'$) as

$$\Delta P' \sim -(\Delta q\,\omega' + q\,\Delta\omega' + \Delta\omega\,q' + \omega\,\Delta q'), \qquad (1)$$

where q, ω, and Δ denote specific humidity at 925 hPa, vertical pressure velocity at 500 hPa (downward motion being positive), and the change from historical to the future, respectively. Variables with and without the prime symbol ($'$) denote the anomalies associated with NW Pacific SLP (represented by regression coefficients against the normalized NW Pacific SLP index) and the climatology in the JJA season, respectively. As the third and fourth terms on the right-hand side of Eq. (1) are much smaller than the first two (Fig. S2), the equation can be further simplified as

$$\Delta P' \sim -(\Delta q\,\omega' + q\,\Delta\omega'). \qquad (2)$$

Figures 5a and 5b show the change in precipitation anomalies and the estimation from Eq. (2) for the ensemble mean of the CESM-LE. The estimation can very well capture the spatial distribution of the change in precipitation anomalies associated with internal IPOC. A further examination of the two right-hand-side terms of Eq. (2) suggests that the change in precipitation is contributed by both the increased background moisture in the lower atmosphere $-\Delta q\,\omega'$ and changes in the anomalous circulation associated with the internal IPOC $-q\,\Delta\omega'$. The two parts are roughly comparable in magnitude over the NW Pacific region, but as the background low-level specific humidity (q) and its change under global warming (Δq) are spatially homogenous (Fig. 5e) in the Indo–western Pacific, the spatial distributions of the two terms are broadly determined by the internal-IPOC-induced anomalous circulation (ω') and its change ($\Delta\omega'$) under global warming (Fig. 5f),

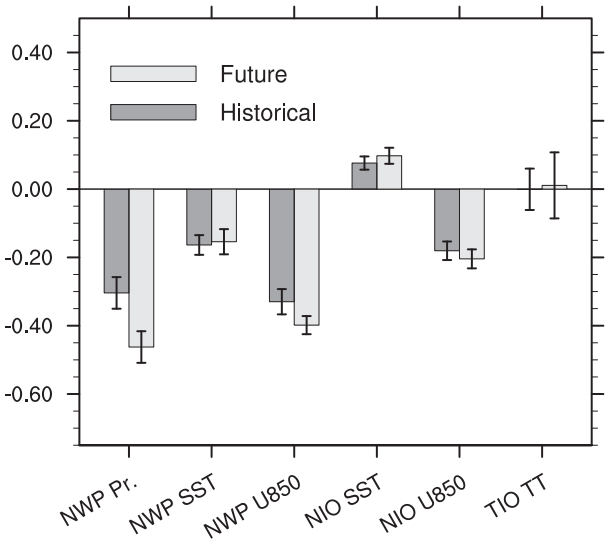

FIG. 4. Anomalies associated with the internal IPOC represented by the regression coefficients of regionally averaged indices of NW Pacific precipitation (averaged over 10°–25°N, 140°–170°E; unit: mm day^{-1}), SST (averaged over 5°–20°N, 140°–170°E; unit: K, scaled by a factor of 2), 850-hPa zonal winds (averaged over 5°–20°N, 140°–170°E; unit: m s^{-1}, scaled by a factor of 0.5), tropical northern IO SST (averaged over 5°–20°N, 50°–120°E; unit: K, scaled by a factor of 2), 850-hPa zonal winds (averaged over 5°–20°N, 50°–120°E; unit: m s^{-1}, scaled by a factor of 0.5), and normalized vertically averaged tropospheric temperature over the tropical IO (15°S–15°N, 60°–110°E; unit: 1) against normalized NW Pacific SLP index (averaged over 10°–35°N, 120°–160°E) in CESM-LE. Error bars indicate intermember standard deviation.

respectively. Specifically, the $-\Delta q\,\omega'$ shows negative change centered around 20°N in the NW Pacific and positive change over the equatorial IO to the Maritime Continent (Fig. 5c) under global warming, corresponding to the descending motion and ascending motion associated with the internal IPOC in the historical simulation (ω'; contours in Fig. 5f), respectively. The distribution of the dynamical component $-q\,\Delta\omega'$ is determined by the change of the vertical motions ($\Delta\omega'$; shading in Fig. 5f), which also features negative changes in the precipitation anomalies over the NW Pacific.

The decomposition explains why the precipitation anomalies associated with the internal IPOC increase while the SST anomalies weaken. The term $\Delta q'$, which is associated with the change in SST anomalies, has a much weaker contribution to the precipitation change compared to the term $-(\Delta q\,\omega' + q\,\Delta\omega')$. Under global warming, the background specific humidity increases ($\Delta q > 0$), allowing the anomalous circulation associated with the internal IPOC to induce more rainfall deficit over the tropical NW Pacific. The decreased rainfall then strengthens the AAC with increased diabatic cooling, further intensifying the circulation anomalies. This enhanced circulation–convection feedback strengthens the internal IPOC in CESM-LE, despite weakened SST anomalies over the tropical NW Pacific.

c. *Weakened NW Pacific SST variability*

We have shown, in section 4a, that the anomalous easterlies on the southern flank of the AAC intensify over the NW Pacific in the future (Fig. 4). According to the WES feedback, the increased wind velocity would induced negative SST anomalies due to enhanced evaporation, but the models have projected otherwise in this region. To understand the change of the SST anomalies, we compute the surface turbulent heat flux anomalies associated with the internal IPOC. Figure 6 shows the change in shortwave radiation and latent heat flux (downward positive), the two dominant terms to the SST anomalies (Fig. S3). The latent heat flux anomalies show no significant change in regions where the anomalous easterlies intensify (Fig. 6b), possibly due to the enhanced Newtonian cooling due to the increased background SST (Xie et al. 2010a; Ying and Huang 2016). The shortwave radiation anomalies, on the other hand, show robust increase over the center and southern flank of the AAC, due to enhanced negative precipitation anomalies (Fig. 6a). The positive shortwave radiation acts to warm the upper ocean, weakening the local negative SST anomalies (Fig. 3). This explains why the enhanced wind anomalies are accompanied by suppressed SST anomalies in the NW Pacific in a warmer climate, indicative of weakened WES feedback, and further shows that local circulation–convection feedback is key to the enhancement of the internal IPOC under global warming.

5. Change of the internal IPOC in CMIP6

a. *Ensemble-mean results*

We first briefly assess the change in the internal IPOC in the CMIP6 ensemble mean. The regression coefficients against the normalized NW Pacific SLP index show a similar distribution to the results of the CESM-LE (Fig. 7; cf. Fig. 3): enhanced SLP and precipitation anomalies centered over the subtropical NW Pacific with enhanced easterlies to the south. The change in the NW Pacific precipitation anomalies has a larger magnitude than that of the SLP (Fig. 8) due to the enhanced background specific humidity according to the precipitation decomposition (Fig. S4). Unlike CESM-LE, CMIP6 captures the interbasin feedback between the positive SST anomalies in the northern IO–South China Sea region and the AAC (Kosaka et al. 2013). This interbasin positive feedback, however, seems largely unchanged according to the insignificant change in the TT anomalies (despite the enhanced SST anomalies) over the tropical IO (Fig. 8), possibly due to the enhanced atmospheric static stability (He et al. 2019). The local WES feedback on the southern flank of the AAC also weakens in the ensemble mean of CMIP6 (Fig. 7e). The strengthened evaporative cooling in the tropical NW Pacific due to the enhanced wind anomalies is overwhelmed by the increased solar insolation associated with the strengthened rainfall deficit (Fig. S5).

We have mentioned in section 3 that the intermember spread of the change in relative vorticity, SLP, and precipitation is much larger in CMIP6 than in CESM-LE (Fig. 2). The same is true for the regression coefficients associated with the internal

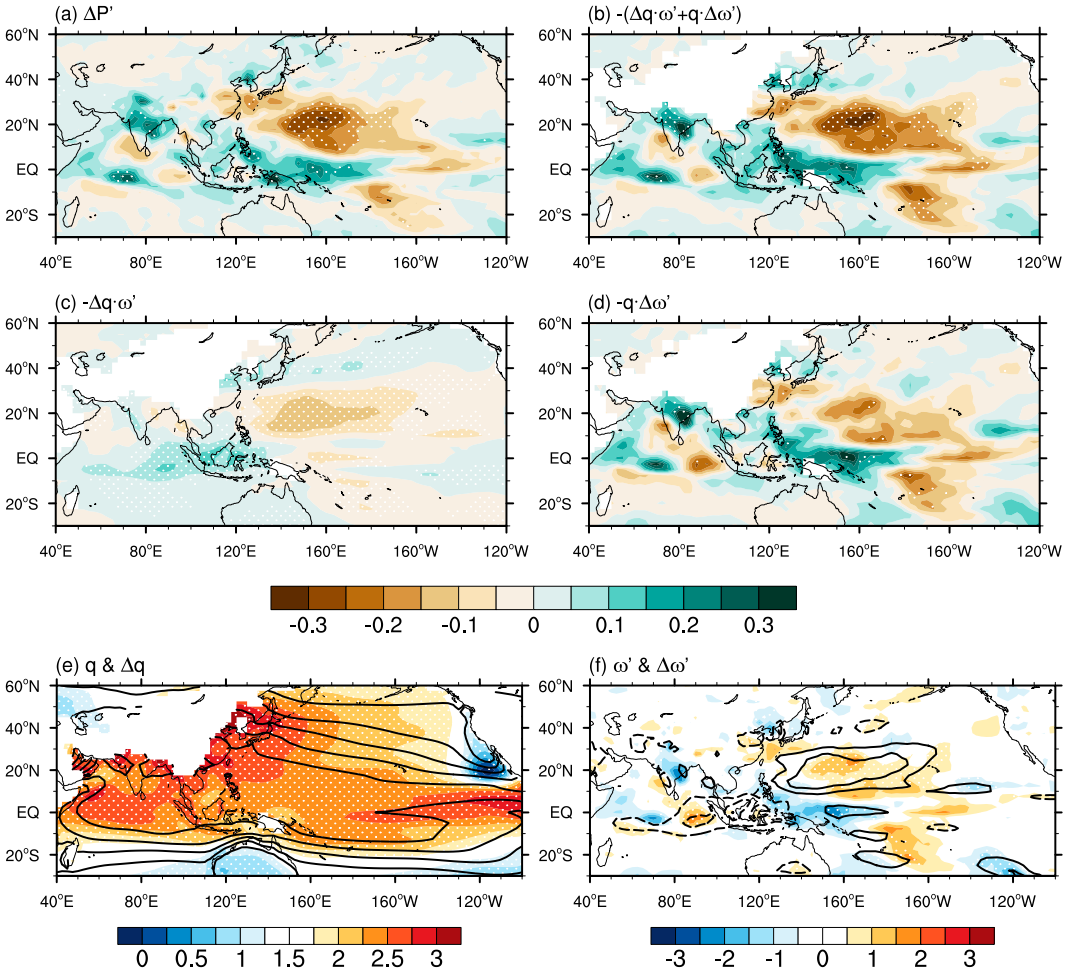

FIG. 5. Ensemble-mean changes in JJA (a) precipitation anomalies (mm day^{-1}) associated with the internal IPOC, (b) estimated precipitation anomalies by Eq. (2), and the two components (c) $-\Delta q\,\omega'$ and (d) $-q\,\Delta\omega'$ in CESM-LE (unit: 10^{-4} Pa s^{-1}). Also shown are ensemble-mean changes of the (e) climatological 925-hPa specific humidity (color shading; unit: g kg^{-1}) and (f) 500-hPa vertical velocity anomalies associated with the internal IPOC (color shading; unit: 10^{-3} Pa s^{-1}) superimposed by their historical values (contours at 6, 8, 10, … g kg^{-1} in (e) and at ±2, ±4, ±6, … $\times 10^{-3}$ Pa s^{-1} in (f)]. Stippling indicates 70% of the members agree on the signs of the changes.

IPOC (Figs. 4 and 8). In the next subsection, we explore the possible mechanisms behind the large intermodel spread.

b. *Intermodel spread*

We have shown that the changes in the internal IPOC, especially those in precipitation anomalies, are strongly tied to the changes in background moisture. To understand the intermodel spread in the projected internal IPOC change, we perform a series of intermodel regressions against the change in the interannual variability of the NW Pacific precipitation ($\Delta P_{\text{S.D.}}$). For each model in the CMIP6 ensemble, the interannual standard deviation of the regionally averaged NW Pacific (10°–25°N, 120°–160°E) precipitation (with ENSO forcing removed) is first calculated in both historical and future simulations, and the changes in standard deviation between the two periods are computed in each model. Finally, $\Delta P_{\text{S.D.}}$ is defined as the normalized departure of the changes in each model relative to the ensemble-mean changes (Fig. 9d). We use the precipitation index because it has the most robust change with the largest intermodel uncertainty among key indices of the internal IPOC (Figs. 4 and 8).

Figure 9 shows the regression of the change in climatological SST relative to the tropical (25°S–25°N) mean (ΔSST^*), specific humidity relative to the tropical mean (Δq^*), precipitation (ΔP), and 850-hPa vector winds ($\Delta\mathbf{V}_{850}$) against the normalized $\Delta P_{\text{S.D.}}$ index. The change in precipitation variability is associated with the change in the background specific humidity in the NW Pacific, consistent with our findings in section 4. The regression coefficient of ΔSST^*, on the other hand, is small in the NW Pacific region. Instead, it shows a zonal dipole distribution in the equatorial Pacific, suggesting that the El Niño–like warming pattern may induce enhanced summer precipitation variability over the NW Pacific via atmospheric teleconnections.

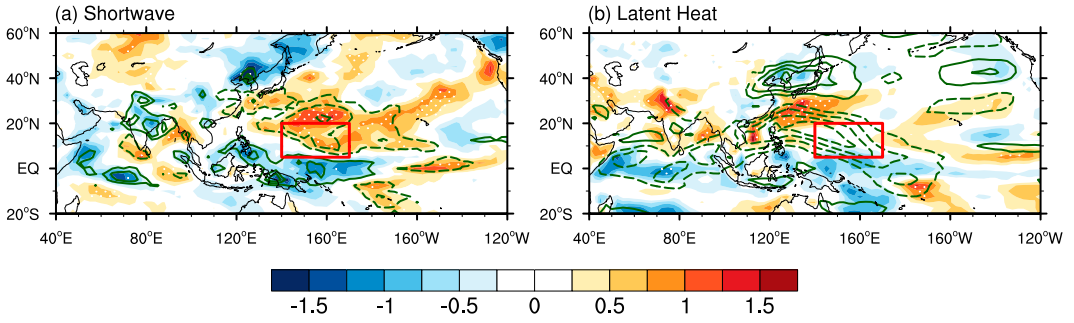

FIG. 6. Ensemble-mean changes in JJA (a) shortwave radiation and (b) latent heat flux anomalies (color shading; unit: W m^{-2}) associated with the internal IPOC, represented by the regression coefficients against normalized NW Pacific SLP index (averaged over 10°–35°N, 120°–160°E) in CESM-LE. Line contours denote the change in (a) precipitation (at ±0.1, ±0.2, … mm day^{-1}) and (b) zonal wind speed anomalies (at ±0.05, ±0.1, … m s^{-1}) associated with the internal IPOC. Stippling indicates 70% of the members agree on the signs of the changes. The red boxes highlight the region where the NW Pacific SST are averaged in Figs. 2 and 4.

The El Niño–like warming pattern weakens the Walker circulation, inducing anomalous descending motion in the Maritime Continent and western equatorial Pacific, suppressing local specific humidity and precipitation (Fig. 9). This further drives an anomalous Hadley cell with anomalous downward motion on the equator and upward motion in the subtropical region of the Northern Hemisphere (Fig. 10). This anomalous upward motion in the NW Pacific enriches the moisture in the lower to middle troposphere and then enhances the internal IPOC by strengthening the convection–circulation feedback as discussed in section 4.

The distribution of the regressions in Fig. 9 bears much resemblance to the ensemble-averaged changes of the climatological SST, specific humidity, low-level winds, and precipitation of both CESM-LE and CMIP6 (not shown). This suggests that changes in the climatological background indeed contribute to those in the ENSO-unrelated interannual variability in the Indo–western Pacific region. Specifically, the seasonal mean

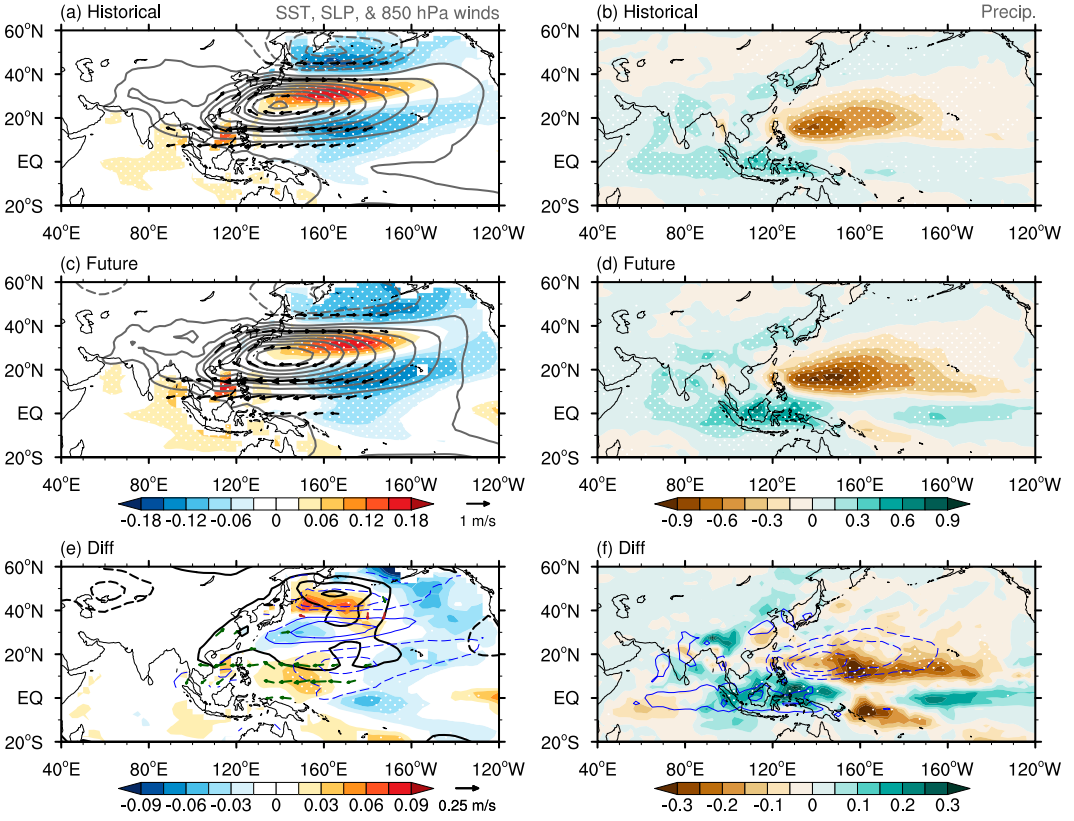

FIG. 7. As in Fig. 3, but for CMIP6 ensemble mean.

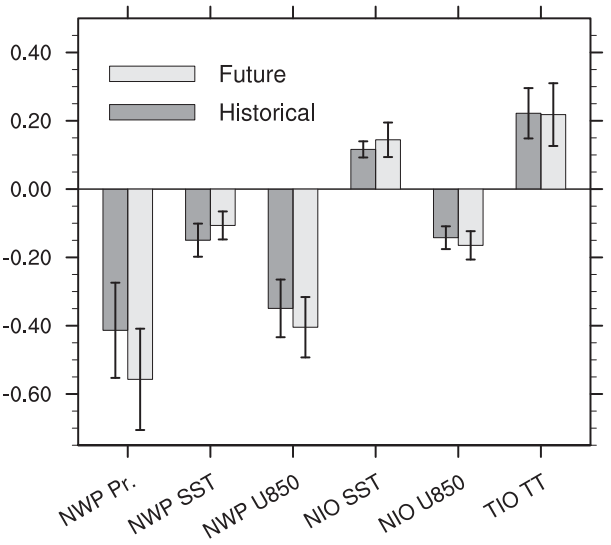

FIG. 8. As in Fig. 4, but for CMIP6. Error bars denote intermodel standard deviation.

background rainfall (ΔP) are also shown to increase (decrease) over the NW Pacific region and equatorial Pacific (Maritime Continent) with respect to increased precipitation variability ($\Delta P_{\mathrm{S.D.}}$). Changes in the climatological precipitations over the NW Pacific are likely due to the combined thermodynamic and dynamic effect as the moisture and upward vertical motion both enhance over that region, while in the deep tropics, the distribution of the precipitation change is determined by the warmer-get-wetter mechanism, inferred from the $\Delta\mathrm{SST}^*$ and ΔP patterns (Xie et al. 2010a; Huang et al. 2013; Long et al. 2016; Geng et al. 2020). The intermodel spread shown in the changes of the precipitation variability may also originate from the intermodel discrepancies in simulating the present-day climatology (S. Zhou et al. 2019). In our case, however, the correlation between the seasonal mean precipitation in the historical simulation (P) and the $\Delta P_{\mathrm{S.D.}}$ index is weak over the Indo–western Pacific region (Fig. S6), further suggesting that the change in the internal IPOC is mainly determined by the change of the mean SST warming pattern.

6. Discussion

This study focuses on the ENSO-unrelated interannual variability, specifically the internal IPOC in the NW Pacific region, but we have also compared the change in ENSO-induced interannual variability over the Indo–western Pacific region (Fig. 11 and Fig. S7). The changes in ENSO-induced interannual variability in rainfall, for example, are actually larger than the ENSO-unrelated counterpart in the ensemble means of CESM-LE and CMIP6. The intermember (or intermodel) spreads (Figs. 11b,e) are also higher for the ENSO-forced IPOC. Note that the mechanism for ensemble spread differs between the CESM-LE and CMIP6. Since CESM-LE is subject to identical radiative forcing, the spread is due to internal modulations (Zheng et al. 2018) while in CMIP6, model physics also contributes. Changes in the ENSO-forced

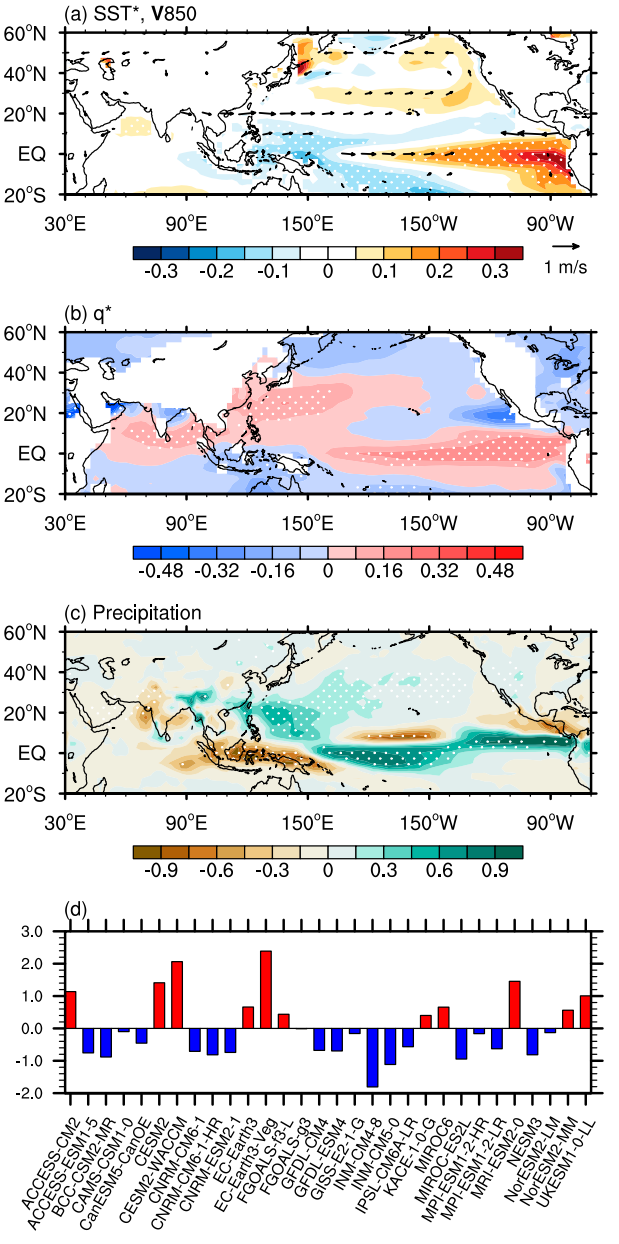

FIG. 9. Intermodel regression coefficients of (a) $\Delta\mathrm{SST}^*$ (shading; unit: K) and $\Delta\mathbf{V}_{850}$ (arrows; unit: m s^{-1}; only significance level > 95% based on the t test are shown), (b) Δq^* (unit: 10^{-3}), and (c) ΔP (unit: mm day^{-1}) against the (d) normalized $\Delta P_{\mathrm{S.D.}}$ index in CMIP6. Stippling indicates regression coefficients > 95% significance level based on the t test.

variability are partly associated with the changes in ENSO amplitude (Figs. 11c,f), suggesting that the uncertainty in ENSO projection contributes to the large intermodel spread of the ENSO-forced IPOC (Wu et al. 2021). The ENSO-unrelated component, on the other hand, is mostly determined by the robust amplification of the background moisture. Indeed, about 1/3 of the models simulate decreased interannual rainfall variability over the NW Pacific region for the ENSO-forced parts in a warmer climate, while 26 of 30 CMIP6 models project an

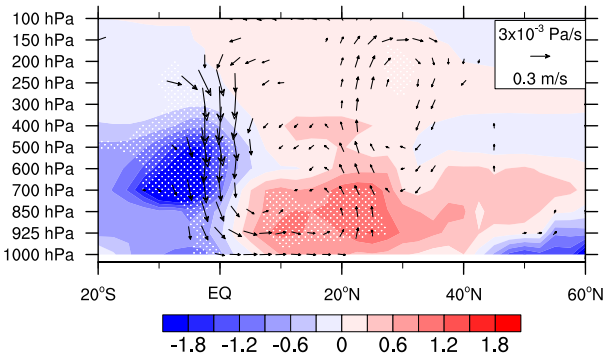

FIG. 10. Vertical cross sections of intermodel regression coefficient of zonally averaged (90°–150°E) meridional wind component and vertical pressure velocity (arrows; only significance level > 95% based on the t test are shown) and Δq^* (shading, with significance level > 95% stippled; unit: 10^{-3}) over the western Pacific against the normalized $\Delta P_{\text{S.D.}}$ index for CMIP6.

increase in the ENSO-unrelated rainfall interannual variability under global warming (Fig. 11b).

Although the internal-IPOC related SST anomalies in the NW Pacific and the subsequent interbasin AAC-IO feedback or local WES feedback do not seem to show a robust enhancement in a warmer climate, the precipitation and circulation anomalies associated with the AAC nevertheless strengthen, indicating strengthened internal IPOC activities. The internal IPOC has large socioeconomic impacts on the populated Indo–western Pacific region. The interannual precipitation variability associated with the internal IPOC is projected to change in East Asia (Figs. 1c and 3f) according to the ensemble mean of the CESM-LE. The precipitation anomalies associated with the internal IPOC show a meridional dipole with negative precipitation anomalies over South China to the tropical NW Pacific and positive anomalies over North China, the Korean Peninsula, and Japan in the historical simulations in CESM-LE. The negative precipitation anomalies are projected to shift northward and intensify (with the magnitude of the change comparable to the historical values; Fig. S8) in a warmer climate. The positive precipitation anomalies over northeastern China and the Korean Peninsula are also projected to intensify. A similar poleward shift of the mei-yu–baiu rainband induced by the internal IPOC can also be seen in the CMIP6. Besides, CESM-LE also simulates an enhanced rainfall anomalies over northern India (Fig. 3; cf. Z.-Q. Zhou et al. 2019). Although the two ensembles disagree somewhat on the exact distribution and intensity of the rainfall anomalies and show some biases compared to observations (see appendix), the enhanced AAC activities associated with the internal IPOC are robust in both ensembles. This indicates that extreme events like the 2020 Yangtze River flooding may occur more frequently with increased intensity in a warmer climate. One may also notice that the precipitation variability induced by the internal IPOC is projected to increase over the southeastern tropical IO off the coast of Sumatra and over the Maritime Continent (Fig. 7f). Such increased rainfall variability is accompanied by decreased seasonal mean background precipitation (Fig. 9c; Lee et al. 2021) due to attenuated Walker circulation, possibly indicating stronger extreme events in a warmer climate. Overall, the intensified internal IPOC calls for more attention to non-ENSO predictors of summer rainfall variability over the Indo–western Pacific region (Lu and Takaya 2021).

7. Summary

Using two state-of-the-art CGCM ensembles, CESM-LE and CMIP6, we have investigated the change in the ENSO-unrelated summer interannual variability over the Indo–western Pacific region under global warming. The two ensemble means show strengthened SLP, low-level circulation, and precipitation variabilities while the SST variability in the NW Pacific and northern IO does not show significant change. A closer look reveals that the relative change in precipitation variability is larger in magnitude than circulation and SLP. The change in the interannual variability is associated with the internal IPOC, characterized by anomalous AAC over the tropical NW Pacific and SST anomalies in the tropical NW Pacific and northern IO.

The AAC is projected to intensify over the NW Pacific region, with strengthened precipitation variability, and easterly wind anomalies on the southern flank. The increased circulation anomalies are due to the enhanced precipitation anomalies, which are further traced back to the increased background water vapor due to global warming following the Clausius–Clapeyron relationship. Enhanced negative precipitation anomalies induce the increased diabatic cooling to intensify the AAC, which in turn strengthens the precipitation anomalies. The relative magnitude of the changes in the precipitation anomalies is larger than the changes in circulation anomalies, likely due to the increased atmospheric static stability in warmer climate.

In the northern IO, the SST anomalies associated with the internal IPOC enhances along with the strengthened easterly anomalies induced by the enhanced AAC. CESM-LE cannot simulate the IO capacitor effect, while in CMIP6 the ensemble mean of the TT anomalies over the tropical IO remains largely unchanged, suggesting a largely unchanged interbasin AAC–IO positive feedback. Over the tropical NW Pacific, the AAC-induced easterlies increase under global warming, but the underlying SST anomalies weaken, suggesting a weakened local WES feedback. The changes of the SST anomalies in the NW Pacific are dominated by the warming effect of the increased solar radiation, due to enhanced negative precipitation anomalies.

The intermodel analysis in CMIP6 suggests that the intensity of the internal IPOC in the future is associated with the change of the background SST, specifically, a dipole pattern in the equatorial Pacific. An El Niño–like warming pattern induces anomalous ascending motion over the NW Pacific by modulation of Walker and Hadley cells. The abundant water vapor induced by the upward motion strengthens the convection–circulation feedback, and hence the internal IPOC activity.

Acknowledgments. We thank three anonymous reviewers for their constructive comments. C.Y.W. and X.T.Z. are supported by the National Natural Science Foundation of China (42205018, 41975092, 42230505), Fundamental Research Funds for the Central Universities (202213047), Shandong Natural Science Foundation Project (ZR2019ZD12), and Taishan Pandeng

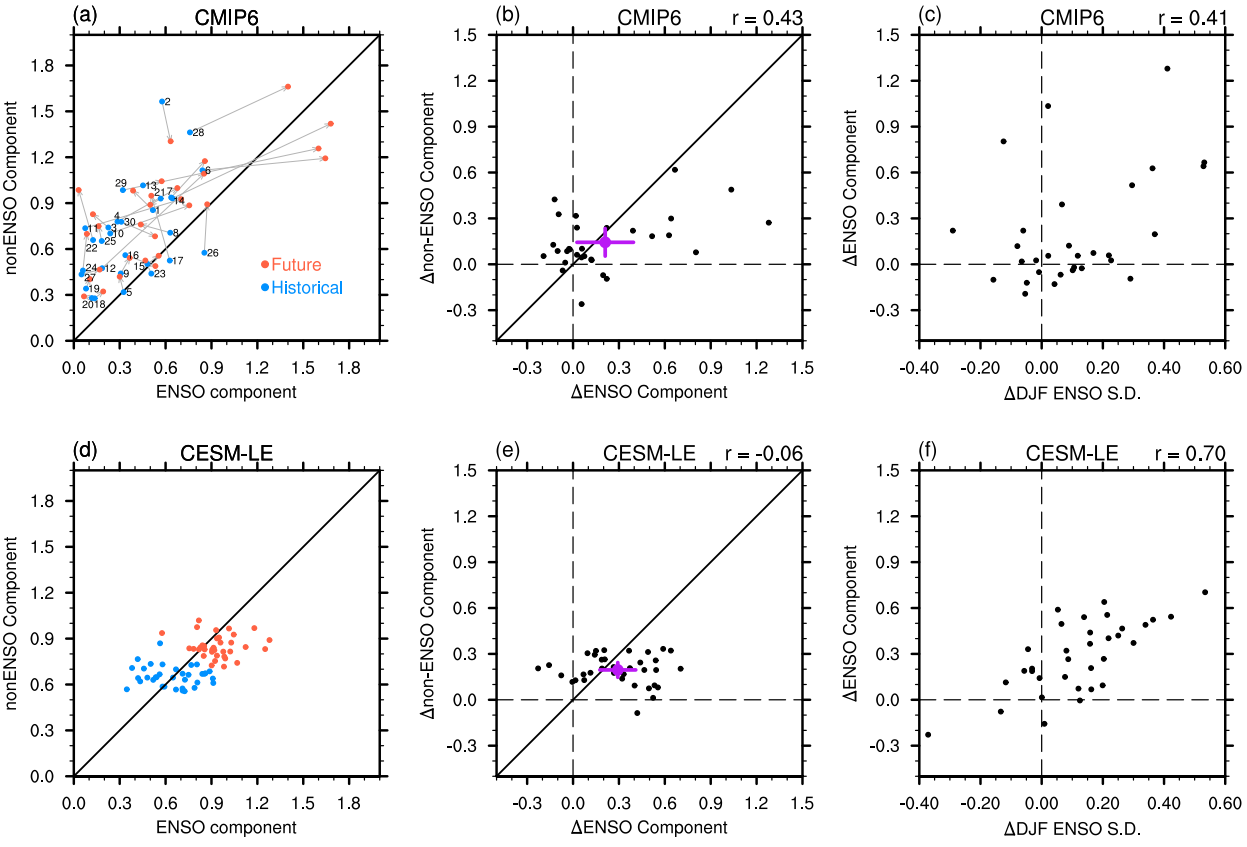

FIG. 11. Scatter diagrams of (a),(d) ENSO-forced and ENSO-unrelated NW Pacific precipitation interannual standard deviation (unit: mm day^{-1}) in historical and future simulations; (b),(e) changes of the ENSO-forced and ENSO-unrelated NW Pacific precipitation interannual standard deviation (unit: mm day^{-1}); (c),(f) changes of the ENSO-forced NW Pacific precipitation interannual standard deviation (unit: mm day^{-1}) against the changes of the DJF Niño-3.4 standard deviation (unit: K) in (top) CMIP6 and (bottom) CESM-LE. Numbers in (a) near the blue dots denote the model numbers in Table 1. Blue and red dots connected by the arrow denote the same model in the historical and future simulations, respectively. Large purple dots and error bars in (b) and (e) denote the ensemble-mean changes and intermember standard deviations, respectively.

Scholar Project. S.P.X. is supported by the National Science Foundation (AGS-2105654).

Data availability statement. The CESM-LE are provided by the CESM Large Ensemble Community Project, hosted on https://www.cesm.ucar.edu/projects/community-projects/LENS/. The CMIP6 data can be downloaded from the PCMDI CMIP6 website (https://pcmdi.llnl.gov/CMIP6/). NCEP–NCAR Reanalysis 1, OISST, and ERSST V5 data are provided by the NOAA PSL, Boulder, Colorado, USA, from their website at https://psl.noaa.gov. ERA5 monthly averaged data on pressure levels and single levels are downloaded at the Copernicus Climate Data Store (https://cds.climate.copernicus.eu).

APPENDIX

Model Evaluation for the Simulation of the ENSO-Forced and Internal IPOC

The appendix evaluates the model's performance in reproducing the ENSO-forced and internal IPOC in the CESM-LE and CMIP6 ensembles. NCEP-NCAR Reanalysis (Kalnay et al. 1996) and Extended Reconstructed SST (ERSST; B. Huang et al. 2017) version 5 covering the period of 1950–99 are used as the reference for the observations, for atmospheric variables and SSTs, respectively. ECMWF Reanalysis version 5 (ERA5; Hersbach et al. 2020) and Optimum Interpolation SST V2 (OISST; Reynolds et al. 2002) covering the period of 1982–2020 are also used for comparison.

a. The ENSO-forced IPOC

The spatial distribution of the ENSO-forced IPOC (Fig. A1) is obtained by the regression of the summer (JJA) SST, SLP, 850-hPa winds, precipitation, and TT against the Niño-3.4 index of the antecedent winter (DJF). From the ensemble-mean perspective, both CESM-LE and CMIP6 can capture the structure of the ENSO-forced IPOC. Specifically, the two ensembles can simulate the anomalous anticyclone (AAC) with suppressed precipitation located in the subtropical northwestern (NW) Pacific, accompanied by positive SST in the tropical IO and

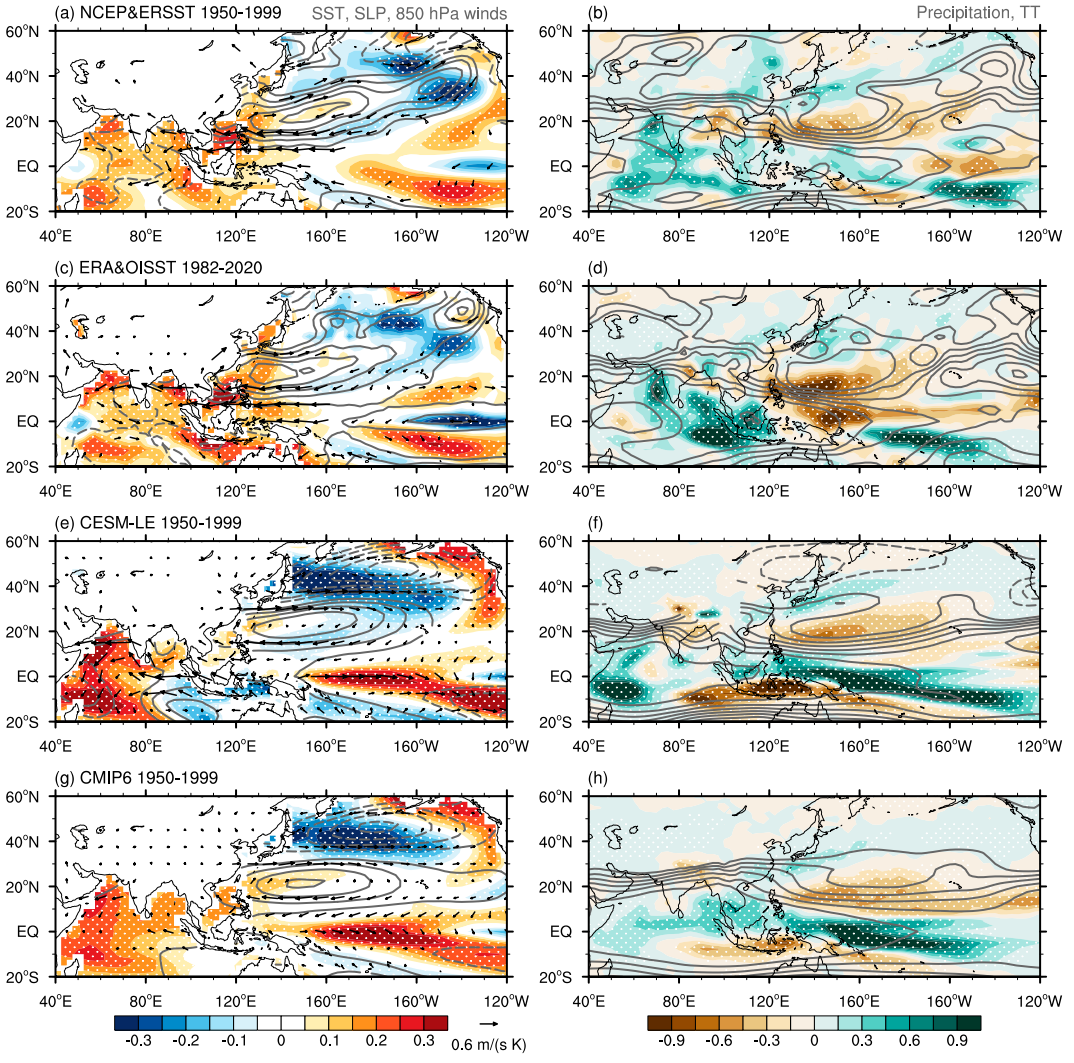

FIG. A1. Structure of the ENSO-forced IPOC in (a)–(d) observations and historical simulations for (e),(f) CESM-LE and (g),(h) CMIP6, represented by the JJA mean regression coefficient of SST (shading in the left column; unit: K K^{-1}), SLP (contours in the left column at ±0.1, ±0.2, ±0.3, … hPa K^{-1}), 850-hPa winds (arrows in the left column), precipitation (shading in the right column; unit: mm day^{-1} K^{-1}), and normalized TT (contours in the right column at ±0.1, ±0.2, ±0.3, … K^{-1}) against DJF mean Niño 3.4 index. Stippling indicates regression coefficients above the 95% significance level based on the *t* test.

negative (statistically significant, albeit weak) SST on the southeastern flank of the AAC. One major discrepancy lies in the equatorial western to central Pacific with biased positive SST anomalies simulated by both ensemble means. Such SST anomalies may weaken the AAC by inducing the Matsuno–Gill response (Fan et al. 2013). Positive SST anomalies in the tropical southeastern Indian Ocean over the Maritime Continent are also very weak in the ensemble mean of CMIP6 and even become negative in the CESM-LE. Correspondingly, the models show positive (negative) precipitation biases in the western equatorial Pacific (southeastern tropical IO). Specifically, positive SST bias in the western to central equatorial IO reduces the zonal gradient of the TT anomalies in the deep tropics over the western Pacific. Other biases include the northeastward extension of the AAC in the midlatitude North Pacific and the SST anomalies in the North Pacific. Overall, the key features of the ENSO-forced IPOC can be reasonably reproduced by the two ensembles.

Next, we inspect the ENSO-forced IPOC in each member of the CESM-LE (Figs. S9 and S10) and CMIP6 ensemble (Figs. S11 and S12). Each member in the CESM-LE ensemble shows remarkable resemblance to the ensemble mean with very small intermember spread. Most members show a high correlation between the JJA NW Pacific SLP and DJF Niño-3.4 index, with only one insignificant at the 95% confidence level. The CMIP6, on the other hand, shows a very strong intermodel spread. Many models cannot even

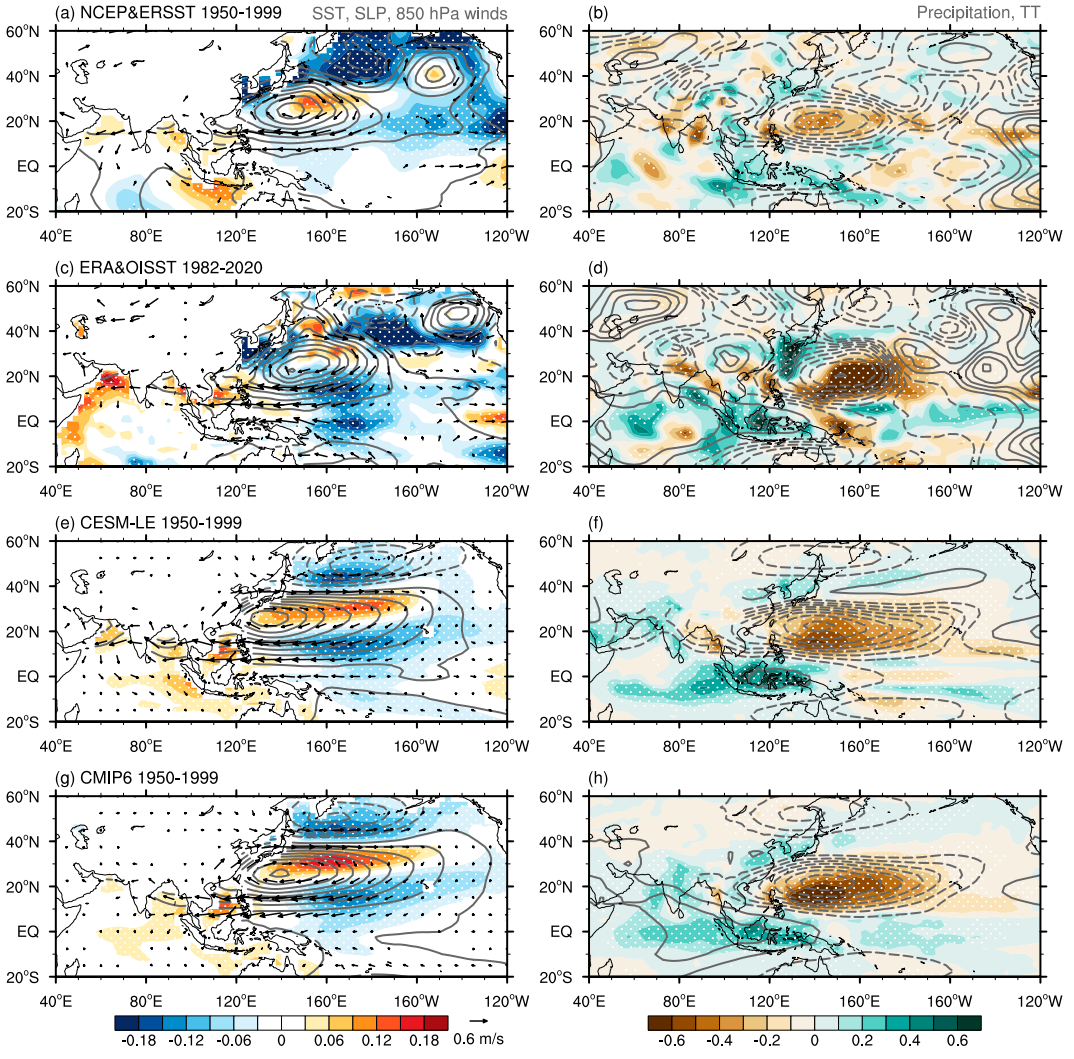

FIG. A2. Structure of the internal IPOC in (a)–(d) the observations and historical simulations for (e),(f) CESM-LE and (g),(h) CMIP6, represented by the JJA mean regression coefficient of SST (shading in the left column; unit: K), SLP (contours in the left column at ±0.1, ±0.2, ±0.3, … hPa), 850-hPa winds (arrows in the left column), precipitation (shading in the right column; unit: mm day^{-1}), and normalized TT (contours in the right column at ±0.1, ±0.2, ±0.3, …) against the normalized NW Pacific SLP index. Stippling indicates regression coefficients above the 95% significance level based on the *t* test.

reproduce the AAC in the ENSO decay summer, despite that almost every model can simulate the positive SST anomalies in the tropical Indian Ocean. The positive SST bias in the equatorial western Pacific can be found in almost every ensemble member in both CESM-LE and CMIP6, suggesting a biased slow decay pace of the simulated ENSO events. Note that among the two models showing negative SST anomalies (ACCESM-CM2 and Kace-1-0-G) in the equatorial western Pacific, the AAC also has the strongest intensity.

b. The internal IPOC

Figure A2 shows the structure of the internal IPOC represented by the regressions against the normalized NW Pacific SLP index (see section 2) where the ENSO-unrelated components are extracted using the regression method described in section 2b. As reported by Wang et al. (2018), the SST anomalies are mostly confined in the tropical NW Pacific, South China Sea, and Bay of Bengal, compared to the ENSO-forced IPOC in both observations and the two ensemble means. The internal IPOC in the observations seems to show some decadal variability as the SST and precipitation anomalies in the tropical NW Pacific and Arabian Sea are much stronger in the period of 1982–2020 compared to the period of 1950–99, possibly due to the shallowed thermocline in the tropical IO (Xie et al. 2010b).

The models are able to capture the AAC and the negative SST anomalies in the tropical NW Pacific with decreased precipitation, which reflect the key ocean–atmosphere interactions as discussed in the main text. The most obvious

model biases in SST anomalies are located in the midlatitude North Pacific, where the two ensembles produce a warm SST bias along 30°N. The models also struggle to reproduce the precipitation anomalies over East Asia and the Indian subcontinent.

Like the case for the ENSO-forced IPOC, the intermember spread of the internal IPOC is quite small (Figs. S13 and S14) in CESM-LE. The intermodel spread for CMIP6 in the internal IPOC, on the other hand, is significantly smaller (Figs. S15 and S16), compared to the ENSO-forced counterpart. Almost all models can reproduce the AAC and the accompanied SST and precipitation anomalies over the tropical NW Pacific. More than half of the models simulate the positive SST anomalies in the tropical northern IO, especially in the South China Sea and Bay of Bengal, evidence of the interbasin positive feedback.

Overall, both CESM-LE and CMIP6 show good skills in reproducing the ENSO-forced and internal IPOC. Especially for the internal IPOC, the intermodel uncertainty in the CMIP6 ensemble reduces dramatically compared to the ENSO-forced counterpart, suggesting that the former is sustained by regional ocean–atmospheric feedback internal to the Indo–western Pacific region, while the latter is highly modulated by ENSO activities. The above analysis justifies the use of the two ensembles to study the change of the internal IPOC in a warmer climate.

REFERENCES

Alexander, M. A., I. Bladé, M. Newman, J. R. Lanzante, N.-C. Lau, and J. D. Scott, 2002: The atmospheric bridge: The influence of ENSO teleconnections on air–sea interaction over the global oceans. *J. Climate*, **15**, 2205–2231, https://doi.org/10.1175/1520-0442(2002)015<2205:TABTIO>2.0.CO;2.

Cai, W., and Coauthors, 2021: Changing El Niño–southern oscillation in a warming climate. *Nat. Rev. Earth Environ.*, **2**, 628–644, https://doi.org/10.1038/s43017-021-00199-z.

Chen, W., J.-Y. Lee, K.-J. Ha, K.-S. Yun, and R. Lu, 2016: Intensification of the western North Pacific anticyclone response to the short decaying El Niño event due to greenhouse warming. *J. Climate*, **29**, 3607–3627, https://doi.org/10.1175/JCLI-D-15-0195.1.

Collins, M., and Coauthors, 2010: The impact of global warming on the tropical Pacific Ocean and El Niño. *Nat. Geosci.*, **3**, 391–397, https://doi.org/10.1038/ngeo868.

Du, Y., S.-P. Xie, G. Huang, and K. Hu, 2009: Role of air–sea interaction in the long persistence of El Niño–induced north Indian Ocean warming. *J. Climate*, **22**, 2023–2038, https://doi.org/10.1175/2008JCLI2590.1.

——, L. Yang, and S.-P. Xie, 2011: Tropical Indian Ocean influence on northwest Pacific tropical cyclones in summer following strong El Niño. *J. Climate*, **24**, 315–322, https://doi.org/10.1175/2010JCLI3890.1.

Eyring, V., S. Bony, G. A. Meehl, C. A. Senior, B. Stevens, R. J. Stouffer, and K. E. Taylor, 2016: Overview of the Coupled Model Intercomparison Project Phase 6 (CMIP6) experimental design and organization. *Geosci. Model Dev.*, **9**, 1937–1958, https://doi.org/10.5194/gmd-9-1937-2016.

Fan, L., S.-I. Shin, Q. Liu, and Z. Liu, 2013: Relative importance of tropical SST anomalies in forcing East Asian summer monsoon circulation. *Geophys. Res. Lett.*, **40**, 2471–2477, https://doi.org/10.1002/grl.50494.

Geng, Y.-F., S.-P. Xie, X.-T. Zheng, and C.-Y. Wang, 2020: Seasonal dependency of tropical precipitation change under global warming. *J. Climate*, **33**, 7897–7908, https://doi.org/10.1175/JCLI-D-20-0032.1.

Gill, A. E., 1980: Some simple solutions for heat-induced tropical circulation. *Quart. J. Roy. Meteor. Soc.*, **106**, 447–462, https://doi.org/10.1002/qj.49710644905.

He, C., T. Zhou, and T. Li, 2019: Weakened anomalous western North Pacific anticyclone during an El Niño–decaying summer under a warmer climate: Dominant role of the weakened impact of the tropical Indian Ocean on the atmosphere. *J. Climate*, **32**, 213–230, https://doi.org/10.1175/JCLI-D-18-0033.1.

——, Z. Cui, and C. Wang, 2022: Response of western North Pacific anomalous anticyclones in the summer of decaying El Niño to global warming: Diverse projections based on CMIP6 and CMIP5 models. *J. Climate*, **35**, 359–372, https://doi.org/10.1175/JCLI-D-21-0352.1.

Held, I. M., and B. J. Soden, 2006: Robust responses of the hydrological cycle to global warming. *J. Climate*, **19**, 5686–5699, https://doi.org/10.1175/JCLI3990.1.

Hersbach, H., and Coauthors, 2020: The ERA5 global reanalysis. *Quart. J. Roy. Meteor. Soc.*, **146**, 1999–2049, https://doi.org/10.1002/qj.3803.

Hu, K., G. Huang, X.-T. Zheng, S.-P. Xie, X. Qu, Y. Du, and L. Liu, 2014: Interdecadal variations in ENSO influences on northwest Pacific–East Asian early summertime climate simulated in CMIP5 models. *J. Climate*, **27**, 5982–5998, https://doi.org/10.1175/JCLI-D-13-00268.1.

——, S.-P. Xie, and G. Huang, 2017: Orographically-anchored El Niño effect on summer rainfall in central China. *J. Climate*, **30**, 10 037–10 045, https://doi.org/10.1175/JCLI-D-17-0312.1.

——, G. Huang, S.-P. Xie, and S.-M. Long, 2019: Effect of the mean flow on the anomalous anticyclone over the Indo-northwest Pacific in post-El Niño summers. *Climate Dyn.*, **53**, 5725–5741, https://doi.org/10.1007/s00382-019-04893-z.

Huang, B., and Coauthors, 2017: Extended Reconstructed Sea Surface Temperature version 5 (ERSSTv5): Upgrades, validations, and intercomparisons. *J. Climate*, **30**, 8179–8205, https://doi.org/10.1175/JCLI-D-16-0836.1.

Huang, P., and S.-P. Xie, 2015: Mechanisms of change in ENSO-induced tropical Pacific rainfall variability in a warming climate. *Nat. Geosci.*, **8**, 922–926, https://doi.org/10.1038/ngeo2571.

——, ——, K. Hu, G. Huang, and R. Huang, 2013: Patterns of the seasonal response of tropical rainfall to global warming. *Nat. Geosci.*, **6**, 357–361, https://doi.org/10.1038/ngeo1792.

——, D. Chen, and J. Ying, 2017: Weakening of the tropical atmospheric circulation response to local sea surface temperature anomalies under global warming. *J. Climate*, **30**, 8149–8158, https://doi.org/10.1175/JCLI-D-17-0171.1.

Jiang, W., G. Huang, P. Huang, and K. Hu, 2018: Weakening of Northwest Pacific anticyclone anomalies during post–El Niño summers under global warming. *J. Climate*, **31**, 3539–3555, https://doi.org/10.1175/JCLI-D-17-0613.1.

——, ——, ——, R. Wu, K. Hu, and W. Chen, 2019: Northwest Pacific anticyclonic anomalies during post-El Niño summers determined by the pace of El Niño decay. *J. Climate*, **32**, 3487–3503, https://doi.org/10.1175/JCLI-D-18-0793.1.

Kalnay, E., and Coauthors, 1996: The NCEP/NCAR 40-Year Reanalysis Project. *Bull. Amer. Meteor. Soc.*, **77**, 437–472,

https://doi.org/10.1175/1520-0477(1996)077<0437:TNYRP>2.0.CO;2.

Kay, J. E., and Coauthors, 2015: The Community Earth System Model (CESM) large ensemble project: A community resource for studying climate change in the presence of internal climate variability. *Bull. Amer. Meteor. Soc.*, **96**, 1333–1349, https://doi.org/10.1175/BAMS-D-13-00255.1.

Kim, S. T., and F.-F. Jin, 2011: An ENSO stability analysis. Part II: Results from the twentieth and twenty-first century simulations of the CMIP3 models. *Climate Dyn.*, **36**, 1609–1627, https://doi.org/10.1007/s00382-010-0872-5.

——, W. Cai, F.-F. Jin, A. Santoso, L. Wu, E. Guilyardi, and S.-I. An, 2014: Response of El Niño sea surface temperature variability to greenhouse warming. *Nat. Climate Change*, **4**, 786–790, https://doi.org/10.1038/nclimate2326.

Klein, S. A., B. J. Soden, and N.-C. Lau, 1999: Remote sea surface temperature variations during ENSO: Evidence for a tropical atmospheric bridge. *J. Climate*, **12**, 917–932, https://doi.org/10.1175/1520-0442(1999)012<0917:RSSTVD>2.0.CO;2.

Knutson, T. R., and S. Manabe, 1995: Time-mean response over the tropical Pacific to increased CO_2 in a coupled ocean–atmosphere model. *J. Climate*, **8**, 2181–2199, https://doi.org/10.1175/1520-0442(1995)008<2181:TMROTT>2.0.CO;2.

Kosaka, Y., S.-P. Xie, N.-C. Lau, and G. A. Vecchi, 2013: Origin of seasonal predictability for summer climate over the northwestern Pacific. *Proc. Natl. Acad. Sci. USA*, **110**, 7574–7579, https://doi.org/10.1073/pnas.1215582110.

Lee, J.-Y., and Coauthors, 2021: Future global climate: Scenario-based projections and near-term information. *Climate Change 2021: The Physical Science Basis*, V. Masson-Delmotte et al., Eds., Cambridge University Press, 553–672.

Long, S.-M., S.-P. Xie, and W. Liu, 2016: Uncertainty in tropical rainfall projections: Atmospheric circulation effect and the ocean coupling. *J. Climate*, **29**, 2671–2687, https://doi.org/10.1175/JCLI-D-15-0601.1.

Lu, B., and Y. Takaya, 2021: Record meiyu-baiu of 2020: Reflections for prediction. *Sci. Bull.*, **66**, 1939–1941, https://doi.org/10.1016/j.scib.2021.05.011.

Ma, J., S.-P. Xie, and Y. Kosaka, 2012: Mechanisms for tropical tropospheric circulation change in response to global warming. *J. Climate*, **25**, 2979–2994, https://doi.org/10.1175/JCLI-D-11-00048.1.

Matsuno, T., 1966: Quasi-geostrophic motions in the equatorial area. *J. Meteor. Soc. Japan*, **44**, 25–43, https://doi.org/10.2151/jmsj1965.44.1_25.

Reynolds, R. W., N. A. Rayner, T. M. Smith, D. C. Stokes, and W. Wang, 2002: An improved in situ and satellite SST analysis. *J. Climate*, **15**, 1609–1625, https://doi.org/10.1175/1520-0442(2002)015<1609:AIISAS>2.0.CO;2.

Wang, B., R. Wu, and X. Fu, 2000: Pacific–East Asian teleconnection: How does ENSO affect East Asian climate? *J. Climate*, **13**, 1517–1536, https://doi.org/10.1175/1520-0442(2000)013<1517:PEATHD>2.0.CO;2.

——, ——, and T. Li, 2003: Atmosphere–warm ocean interaction and its impacts on Asian-Australian monsoon variation. *J. Climate*, **16**, 1195–1211, https://doi.org/10.1175/1520-0442(2003)16<1195:AOIAII>2.0.CO;2.

——, B. Q. Xiang, and J.-Y. Lee, 2013: Subtropical high predictability establishes a promising way for monsoon and tropical storm predictions. *Proc. Natl. Acad. Sci. USA*, **110**, 2718–2722, https://doi.org/10.1073/pnas.1214626110.

Wang, C.-Y., S.-P. Xie, and Y. Kosaka, 2018: Indo-western Pacific climate variability: ENSO forcing and internal dynamics in a tropical Pacific pacemaker simulation. *J. Climate*, **31**, 10 123–10 139, https://doi.org/10.1175/JCLI-D-18-0203.1.

——, ——, and ——, 2020: ENSO-unrelated variability in Indo–northwest Pacific climate: Regional coupled ocean–atmospheric feedback. *J. Climate*, **33**, 4095–4108, https://doi.org/10.1175/JCLI-D-19-0426.1.

Wang, X., S.-P. Xie, Z. Guan, and M. Wang, 2021: A common base mode of Asian summer monsoon variability across timescales. *J. Climate*, **34**, 7359–7371, https://doi.org/10.1175/JCLI-D-20-0856.1.

Wu, M., T. Zhou, X. Chen, and B. Wu, 2020: Intermodel uncertainty in the projection of the anomalous western North Pacific anticyclone associated with El Niño under global warming. *Geophys. Res. Lett.*, **47**, e2019GL086139, https://doi.org/10.1029/2019GL086139.

——, ——, and ——, 2021: The source of uncertainty in projecting the anomalous western North Pacific anticyclone during El Niño–decaying summers. *J. Climate*, **34**, 6603–6617, https://doi.org/10.1175/JCLI-D-20-0904.1.

Wu, R. G., B. P. Kirtman, and V. Krishnamurthy, 2008: An asymmetric mode of tropical Indian Ocean rainfall variability in boreal spring. *J. Geophys. Res.*, **113**, D05104, https://doi.org/10.1029/2007JD009316.

Xie, S.-P., 2023: *Coupled Atmosphere–Ocean Dynamics: From El Niño to Climate Change*. Elsevier, 400 pp.

——, H. Annamalai, F. A. Schott, and J. P. McCreary Jr., 2002: Structure and mechanisms of south Indian Ocean climate variability. *J. Climate*, **15**, 864–878, https://doi.org/10.1175/1520-0442(2002)015<0864:SAMOSI>2.0.CO;2.

——, K. Hu, J. Hafner, H. Tokinaga, Y. Du, G. Huang, and T. Sampe, 2009: Indian Ocean capacitor effect on Indo-western Pacific climate during the summer following El Niño. *J. Climate*, **22**, 730–747, https://doi.org/10.1175/2008JCLI2544.1.

——, C. Deser, G. A. Vecchi, J. Ma, H. Teng, and A. T. Wittenberg, 2010a: Global warming pattern formation: Sea surface temperature and rainfall. *J. Climate*, **23**, 966–986, https://doi.org/10.1175/2009JCLI3329.1.

——, Y. Du, G. Huang, X. Zheng, H. Tokinaga, K. Hu, and Q. Liu, 2010b: Decadal shift in El Niño influences on Indo–western Pacific and East Asian climate in the 1970s. *J. Climate*, **23**, 3352–3368, https://doi.org/10.1175/2010JCLI3429.1.

——, Y. Kosaka, Y. Du, K. Hu, J. S. Chowdary, and G. Huang, 2016: Indo-western Pacific Ocean capacitor and coherent climate anomalies in post-ENSO summer: A review. *Adv. Atmos. Sci.*, **33**, 411–432, https://doi.org/10.1007/s00376-015-5192-6.

Yang, J., Q. Liu, S.-P. Xie, Z. Liu, and L. Wu, 2007: Impact of the Indian Ocean SST basin mode on the Asian summer monsoon. *Geophys. Res. Lett.*, **34**, L02708, https://doi.org/10.1029/2006GL028571.

Yeh, S.-W., J.-S. Kug, B. Dewitte, M.-H. Kwon, B. P. Kirtman, and F.-F. Jin, 2009: El Niño in a changing climate. *Nature*, **461**, 511–514, https://doi.org/10.1038/nature08316.

Ying, J., and P. Huang, 2016: Cloud–radiation feedback as a leading source of uncertainty in the tropical Pacific SST warming pattern in CMIP5 models. *J. Climate*, **29**, 3867–3881, https://doi.org/10.1175/JCLI-D-15-0796.1.

——, ——, T. Lian, and D. Chen, 2019: Intermodel uncertainty in the change of ENSO's amplitude under global warming: Role of the response of atmospheric circulation to SST anomalies. *J. Climate*, **32**, 369–383, https://doi.org/10.1175/JCLI-D-18-0456.1.

Zhang, R. H., A. Sumi, and M. Kimoto, 1996: Impact of El Niño on the East Asian monsoon: A diagnostic study of the '86/87 and '91/92 events. *J. Meteor. Soc. Japan*, **74**, 49–62, https://doi.org/10.2151/jmsj1965.74.1_49.

Zheng, X.-T., 2019: Indo-Pacific climate modes in warming climate: Consensus and uncertainty across model projections. *Curr. Climate Change Rep.*, **5**, 308–321, https://doi.org/10.1007/s40641-019-00152-9.

——, S.-P. Xie, G. A. Vecchi, Q. Liu, and J. Hafner, 2010: Indian Ocean dipole response to global warming: Analysis of ocean–atmospheric feedbacks in a coupled model. *J. Climate*, **23**, 1240–1253, https://doi.org/10.1175/2009JCLI3326.1.

——, ——, and Q. Liu, 2011: Response of the Indian Ocean basin mode and its capacitor effect to global warming. *J. Climate*, **24**, 6146–6164, https://doi.org/10.1175/2011JCLI4169.1.

——, C. Hui, and S.-W. Yeh, 2018: Response of ENSO amplitude to global warming in CESM large ensemble: Uncertainty due to internal variability. *Climate Dyn.*, **50**, 4019–4035, https://doi.org/10.1007/s00382-017-3859-7.

——, J. Lu, and C. Hui, 2021: Response of seasonal phase locking of Indian Ocean Dipole to global warming. *Climate Dyn.*, **57**, 2737–2751, https://doi.org/10.1007/s00382-021-05834-5.

Zhou, S., P. Huang, G. Huang, and K. Hu, 2019: Leading source and constraint on the systematic spread of the changes in East Asian and western North Pacific summer monsoon. *Environ. Res. Lett.*, **14**, 124059, https://doi.org/10.1088/1748-9326/ab547c.

Zhou, Z.-Q., S.-P. Xie, and R. Zhang, 2019: Interannual variability of summer surface air temperature over central India: Implications for monsoon onset. *J. Climate*, **32**, 1693–1706, https://doi.org/10.1175/JCLI-D-18-0675.1.

——, ——, and ——, 2021: Historic Yangtze flooding of 2020 tied to extreme Indian Ocean conditions. *Proc. Natl. Acad. Sci. USA*, **118**, e2022255118, https://doi.org/10.1073/pnas.2022255118.